Dipole and spin-dipole resonances in charge-exchange reactions on ^{12}C

X. Yang, L. Wang, and J. Rapaport

Ohio University, Athens, Ohio 45701

C. D. Goodman, C. Foster, Y. Wang, and W. Unkelbach

Indiana University, Indiana University Cyclotron Facility, Bloomington, Indiana 47405

E. Sugarbaker, D. Marchlenski, S. de Lucia, and B. Luther

Ohio State University, Columbus, Ohio 43210

J. L. Ullmann, A. G. Ling, B. K. Park, D. S. Sorenson,
L. Rybarcyk, and T. N. Taddeucci

Los Alamos National Laboratory, Los Alamos, New Mexico 87545

C. R. Howell and W. Tornow

Department of Physics, Duke University and Triangle Universities Nuclear Laboratory, Durham, North Carolina 27706

The ^{12}C$(n,p)^{12}$B reaction was studied using the white neutron source at the Los Alamos Meson Physics Facility/Weapons Neutron Research center with a continuous incident neutron energy from 60 to 260 MeV. Double differential cross sections were measured in the angular range $11° \leq \theta_{lab} \leq 37°$. Using the neutron time-of-flight facility at the Indiana University Cyclotron Facility, we also studied the ^{12}C$(p,n)^{12}$N reaction at $E_p = 186$ MeV and the ^{12}C$(\vec{p},\vec{n})^{12}$N reaction at $E_{\vec{p}} = 160$ and 186 MeV. Double differential cross sections were measured between $\theta_{lab} = 0°$ and $\theta_{lab} = 50°$ in 5° steps. Spin observables D_{NN}, A_Y, and P were measured at $\theta_{lab} = 5°, 9°, 13°$ with $E_{\vec{p}} = 160$ MeV and $\theta_{lab} = 15°, 20°$ with $E_{\vec{p}} = 186$ MeV. Angular distributions of differential cross section and spin observables for low-lying transitions in the residual nuclei are compared with distorted-wave impulse approximation (DWIA) calculations. A multipole decomposition analysis was performed to study the giant dipole and giant spin-dipole resonances. The contributions of the quasifree reaction in the giant resonance region were subtracted. The empirical results of energy distributions for dipole ($\Delta L = 1$) transition are compared with DWIA calculations using nuclear structure information obtained with a conventional shell model and also with a random phase approximation.

PACS number(s): 25.40.Hs, 27.40.+z

I. INTRODUCTION

In a simple model, giant resonances can be described as excitation modes of collective motion or vibration of nucleons inside the nucleus. Giant resonances may also be interpreted microscopically as the result of a coherent superposition of many one-particle, one-hole ($1p$-$1h$) excitations. In this model, the theoretical evaluation of these resonances becomes practical in a case such as the ^{12}C nucleus for which the number of particle-hole configurations is not too large.

The nucleon charge-exchange reaction is a useful probe to study the isovector response in nuclei [1] and to excite giant resonances. From a theoretical point of view [1, 2], one interesting aspect of using this probe is the study of spin-isovector ($\sigma\tau$) and isovector (τ) nuclear responses that characterize the giant resonances. At intermediate energies and low momentum transfer, the $\sigma\tau$ interaction plays a dominant role and is almost energy independent in the energy range from about 100 to 500 MeV. On the other hand, the τ interaction has a rather strong energy

dependence. This interaction strength decreases rapidly with increasing energy in the range between 50 and 200 MeV and then remains almost constant up to 500 MeV [1, 2].

A number of reports have been published on studies of the ground state (g.s.) Gamow-Teller (GT) ($\Delta L = 0, \Delta S = 1$) transition in the ^{12}C$(p,n)^{12}$N reaction [3–8] as well as in the ^{12}C$(n,p)^{12}$B reaction [8–12]. A study of isospin symmetry in nucleon scattering from ^{12}C at 280 MeV has been done by Mildenberger *et al.* [8], by exciting the ($T = 1$, $J^\pi = 1^+$) triplet isospin states: ^{12}N(g.s.), ^{12}B(g.s.), and ^{12}C(15.1 MeV).

The transitions to the members of the isospin triplet from the g.s. of ^{12}C are characterized by an angular momentum transfer $\Delta L = 0$. These transitions dominate the observed charge-exchange spectra at small momentum transfer [4, 11]. However, at a larger momentum transfer, $q \approx 0.5$ fm^{-1}, the spectra are dominated by transitions characterized by an angular momentum transfer $\Delta L = 1$. Two broad structures centered at around 4 MeV and 7 MeV excitation energy in either ^{12}N or

48   1158

^{12}B have been interpreted as superpositions of collective states mainly of spin dipole ($\Delta L = 1, \Delta S = 1$) (GSDR) or dipole ($\Delta L = 1, \Delta S = 0$) (GDR) transitions, respectively [9, 12–15]. Several authors [9, 12–15] report simple shell-model calculations assuming the above character of these resonances and indicate a good agreement with experimental results.

Other reactions have also been used to study isovector transitions on the mass $A = 12$ system such as the ^{12}C(γ, π^+)^{12}B [16], ^{12}C(γ, n)^{11}C [17], ^{12}C(^{3}He,t)^{12}N [18], and ^{12}C($d,^2$He)^{12}B [19]. More recently, heavy ion reactions have been used to induce charge-exchange transitions on ^{12}C target [20–22], to selectively excite either spin-transfer ($\Delta S = 1$) or non-spin-transfer ($\Delta S = 0$) transitions. However, in the analysis of the heavy ion reactions, the internal structure of the projectile and the interaction between the complex projectile and the nucleus have to be considered, complexities which are not present in nucleon charge-exchange reactions such as ^{12}C(p, n)^{12}N or ^{12}C(n, p)^{12}B reactions.

The advantage of a continuous energy neutron source, such as the one available at Los Alamos Meson Physics Facility/Weapons Neutron Research Center (LAMPF/WNR) [23] is the ability to study in a single experiment, the energy dependence of the spin-isospin nuclear interaction. We have used the LAMPF/WNR facilities to measure the ^{12}C(n, p)^{12}B reaction in the energy range between 60 and 260 MeV and in the angular range of $11° \leq \theta_{\text{lab}} \leq 37°$. We have also used the time-of-flight facility at the Indiana University Cyclotron Facility (IUCF) to measure differential cross sections for the ^{12}C(p, n)^{12}N reaction at 186 MeV in the angular range $0° \leq \theta_{\text{lab}} \leq 50°$. In the latter study we also analyzed the spin-isospin response in the quasifree (QF) region, which becomes important at energies higher than 150 MeV [24].

We have characterized the observed differential cross section for the ^{12}C(p, n)^{12}N reaction in the QF region, at angles $\theta_{\text{lab}} \geq 25°$, via an empirical function [25, 26]. This function was extrapolated to forward angles to estimate the QF contribution in the region where giant resonances are predominant. A similar procedure was used in the ^{12}C(n, p)^{12}B analysis.

Polarization observables for $T = 1$ states have been reported in the ^{12}C($\vec{p}, \vec{p}'$)^{12}C reaction at intermediate energies [28–30]. Analyzing power data for several isovector transitions were measured [30] at 200 MeV up to a momentum transfer of 2.8 fm^{-1}. Analyzing power data were also obtained in the ^{12}C($d,^2$He)^{12}B reaction [19] at 70 MeV incident energy for excited states in ^{12}B up to 5 MeV. The ^{12}C($\vec{p}, \vec{n}$)^{12}N reaction has been previously reported at $E_{\vec{p}} = 160$ MeV [31, 32]. The analyzing powers have been measured for the g.s. and the first excited state at several angles. The $0°$ transverse polarization transfer coefficient $D_{NN}(0°)$ for the g.s. transition has been reported by Taddeucci et al. [32]. For the first time we present polarization observable data for the reaction ^{12}C($\vec{p}, \vec{n}$)^{12}N at angles other than zero degree for the g.s. and states in ^{12}N centered at 4 MeV and 7 MeV. The data were taken at $E_{\vec{p}} = 160$ MeV and 186 MeV. We present angular distributions for these low-lying transitions and the excitation energy distribution for different

multipolarities, up to 25 MeV excitation energy.

A multipole decomposition analysis (MDA) [33, 34] was applied to study the giant resonances. In particular, we obtained the excitation energy distribution of the transitions characterized with the angular momentum transfer $\Delta L = 1$. These results are compared with the results from $1p$-$1h$ shell-model calculations and with the results from a more sophisticated calculation using random phase approximation (RPA).

II. EXPERIMENTAL SETUP

The experiments described in this paper were done at two different facilities. A brief description of each experimental setup is presented below. For a more complete description of the IUCF neutron time-of-flight facility, the reader is referred to Refs. [35, 36], while for the LAMPF/WNR facility we cite Refs. [23, 34, 37–39].

A. Experimental setup at IUCF

The ^{12}C(p, n)^{12}N experiment was carried out at the IUCF neutron time-of-flight facility. Differential cross sections were measured with an unpolarized proton beam of 186 MeV. For the polarization observable measurements the data were obtained with a transverse polarized proton beam at energies of 160 MeV and 186 MeV.

With respect to the undeflected proton beam, two detector stations were located on the $0°$ and $24°$ lines, 101 m and 62 m away from the target, respectively. For the cross-section measurements, in each detector station, six 102 cm $\times$ 10 cm $\times$ 15 cm NE102 detectors were stacked together forming a detection plane with the long dimension along the scattered beam axis. With both detector stations we were able to cover an angular range from $\theta_{\text{lab}} = 0°$ to $50°$. The observed neutron energy resolution was about 1 MeV for the $0°$ detector station at 101 m and about 1.5 MeV for the $24°$ detector station at 62 m.

Two measurements of polarization observables were also performed at incident proton energies of 160 MeV and 186 MeV by using the IUCF neutron polarimeter [36]. Two parallel neutron detector planes separated by 100 cm, and perpendicular to the flight path, were formed with the same NE102 scintillators used in the differential cross-section measurements. Each plane consisted of six NE102 detectors. Only the zero degree neutron detector station was used in this setup. The flight path was 76.5 m (71.0 m) for the measurements of incident proton energy at $E_{\vec{p}} = 186$ MeV (160 MeV). For the data analysis, a valid event was defined as the neutron scattered from the hydrogen atoms in the first neutron detector plane and detected again in the second plane. A thin NE102 scintillator was used as a charged particle detector. It was located in front of the second detector plane to eliminate forward going protons from back angle n-p scattering which have a very low analyzing power. Photomultiplier tubes were located at both ends of each scintillator. The time difference between the signals from the two ends of the scintillator was used to determine the position of events. By keeping track of which detector was

triggered, the (x, y) coordinates of events in both planes were determined and the n-p scattering angles (θ, ϕ) were evaluated.

With the swinger in use, data for the normal polarization transfer coefficient (D_{NN}), the analyzing power (A_Y), and the induced polarization (P) were obtained at $\theta_{\text{lab}} = 15°$ and $20°$ with a 93.8 mg/cm^2 thick $^{\text{nat}}$C target at an incident energy of 186 MeV. Data at $\theta_{\text{lab}} = 5°$, $9°$, and $13°$ were measured with a 185.5 mg/cm^2 thick $^{\text{nat}}$C target at an incident energy of 160 MeV. At nonzero scattering angles, the neutron intensity and polarization may vary with scattering angle so that the intensity and spin might not be the same over the extent of the face of the polarimeter, introducing a left-right asymmetry that is not due to the spin being measured. A superconducting solenoid was used in the neutron flight path to periodically reverse the neutron spin in order to empirically evaluate the instrumental asymmetry. Additional information of the experimental setup and the function of the superconducting solenoid is described in Ref. [40].

B. Experimental setup at LAMPF/WNR

The differential cross section for the ^{12}C$(n, p)^{12}$B reaction was measured using the LAMPF/WNR white neutron source [23]. Neutrons of continuous energies from 60 to 260 MeV were used for this study. The detection system has been previously described in Refs. [34, 37–39]. Only a brief account is presented here. The target-detector station was located at approximately 90 m away from the neutron production target. The neutron beam was collimated to a size of 10 cm × 10 cm and after passing through two charged particle veto wire chambers it entered the target array. The targets were positioned in a multitarget array (a combination of four targets and four wire chambers) similar to the one described by Henderson *et al.* [41]. The four wire chambers provided target identification for scattered charged particle events. Beyond the target array, two large drift chambers were placed to trace the scattered charged particles. A large thin plastic scintillator used as a ΔE detector was located in front of a calorimeter wall which consisted of 15 identical CsI crystals arranged in 3 rows and 5 columns and used as the E detectors. The E-ΔE detectors provided charged particle identification information and with the E detectors we measured the energy of outgoing particles. Three carbon targets (1) $^{\text{nat}}$C (187 mg/cm^2, 9.5×11.2 cm^2); (2) $^{\text{nat}}$C (249 mg/cm^2, 9.2×12.3 cm^2); (3) $^{\text{nat}}$C (278 mg/cm^2, 15.3×15.2 cm^2) and one CH$_2$ target (76 mg/cm^2, 12.0×12.0 cm^2) were used in this experiment. The well-known H(n, p) differential cross sections [42] and the data obtained from the CH$_2$ target were used for normalization purposes. The angular range of this experiment covers θ_{lab} from $11°$ to $37°$. The forward angle data (from $0°$ to $7°$) for the ^{12}C$(n, p)^{12}$B reaction were measured by Sorenson *et al.* [11, 37] using the same experimental facility.

III. ANALYSIS OF DATA

Different data analysis procedures were used for the two sets of data reported in this study. They are described in the following subsections.

A. The ^{12}C$(p, n)^{12}$N data analysis

Several instrumental calibration procedures were done prior to data reduction. They are the calibrations for pulse height, calibrations for longitudinal position of an event, and calibrations for time of flight in each of the detectors. These calibrations were done using cosmic ray pulses defined by a coincidence event of all six detectors as described in more detail in Refs. [40, 43]. Absolute differential cross sections were obtained by normalizing the data to the well-known differential cross section of the ^{7}Li$(p, n)^7$Be(g.s.+0.43 MeV) transitions [44]. Data with a ^{7}Li target were obtained using the same setup. We also measured the differential cross section for the ^{13}C$(p, n)^{13}$N reaction using a 99% enriched ^{13}C target. The data were utilized to obtain an overall time-of-flight calibration using the well-known excited states in ^{13}N and to subtract the 1.11% of ^{13}C contamination in the spectra obtained with the $^{\text{nat}}$C target. The spectra obtained at $\theta_{\text{lab}} = 5°$ and $25°$ for the ^{12}C$(p, n)^{12}$N reaction at 186 MeV are presented in Fig. 1. The fitting procedures are described in Sec. IV B.

A detailed information about the data analysis used in the measurement of spin observables is presented in Ref. [40].

B. The ^{12}C$(n, p)^{12}$B data analysis

The techniques reported in Refs. [37, 38, 45] were used for the instrumental calibrations of the present experiment. The obtained efficiencies of the target wire chambers were about 93% to 98%. Therefore some of the
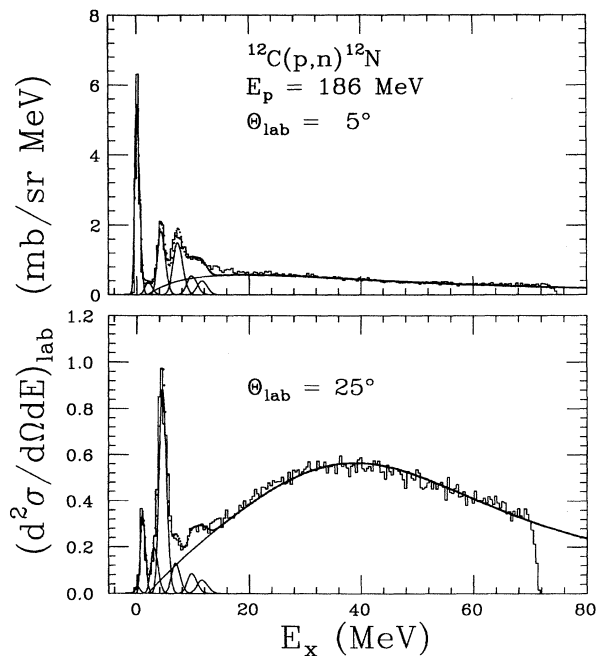
FIG. 1. Excitation energy spectra for the ^{12}C$(p, n)^{12}$N at $E_p = 186$ and $\theta_{\text{lab}} = 5°$ and $25°$. The fitting procedures are described in text.

events in targets 2, 3, and 4 were misidentified. Corrections for these misidentified events and background subtraction were done by following the procedures described in Refs. [34, 39]. The solid angle acceptance for each target was calculated by a Monte Carlo simulation code MAGPLT [37, 46]. The absolute differential cross sections for transitions measured in the $^{12}C(n,p)^{12}B$ reaction were obtained via normalization to the $H(n,p)$ absolute differential cross section [42]. In order to increase the statistics, the data for incident energies E_n less than 100 MeV have been binned in 10-MeV intervals, the data of E_n greater than 100 MeV have been binned in 20-MeV intervals, and the angular bin size has been set to 2°. The obtained proton energy resolution is neutron energy dependent and is about 1.5 MeV for neutron energies between 60 and 70 MeV and about 3.0 MeV for neutron energies between 180 and 200 MeV. The spectra at three different incident energies and at $\theta_{lab} = 10° - 12°$ are shown in Fig. 2. The fitting procedure is described in the Sec. IV B.

IV. RESULTS

The nucleon charge-exchange $^{12}C(p,n)^{12}N$ and $^{12}C(n,p)^{12}B$ reactions, for a target with isospin $T = 0$ such as ^{12}C, excite isobaric analog final states in ^{12}N and ^{12}B for which the same differential cross section is expected at the same incident nucleon energy. Differences in distortion and Coulomb effects are in general small at intermediate incident energies. In this section we present angular distribution results for the $^{12}C(p,n)^{12}N$ reaction
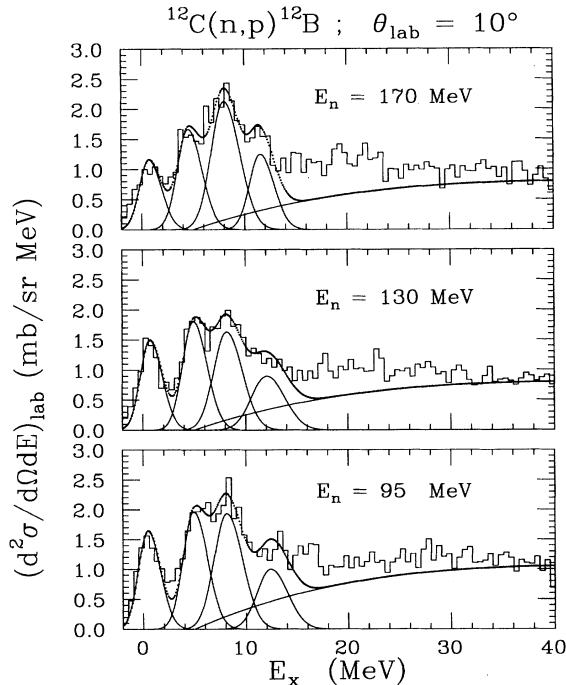
FIG. 2. Excitation energy spectra for the $^{12}C(n,p)^{12}N$ at $\theta_{lab} = 10°$ and E_n=170, 130, and 95 MeV. The fitting procedures are described in text.

and compare with those to analog transitions obtained in the $^{12}C(n,p)^{12}B$ reaction at similar incident energies. We also present spin observables obtained in the $^{12}C(\vec{p},\vec{n})^{12}N$ for the low-lying transitions. These results are compared with distorted wave impulse approximation (DWIA) calculations. Since at incident energies above 150 MeV and at high energy loss the quasifree process is dominant in the measured spectra, we have estimated its tail contribution in the region of the giant dipole and spin dipole resonances. Results are also presented using a multipole decomposition analysis [33, 34] in the excitation energy region above 2.5 MeV and up to 25 MeV. Finally the measured differential cross section spectra are compared with DWIA calculations.

A. DWIA calculations

The microscopic DWIA calculations were carried out using the computer code DW81 [47]. In these calculations, the knock-out exchange amplitudes are treated exactly.

For the interaction between the incident and struck nucleon, we used the free nucleon-nucleon interaction as parametrized by Franey and Love [48]. The set of interaction parameters corresponding to a slightly higher energy than the incident nucleon energy were consistently used in the calculations. For instance, the parameters reported at $E = 210$ MeV were used in the DWIA calculations for both the $^{12}C(p,n)^{12}N$ reaction measured at $E_p = 186$ MeV and for the $^{12}C(n,p)^{12}B$ measured at $E_n = 190$ MeV.

For the nuclear structure part, the shell-model code OXBASH [49] was used to calculate the $1p$-$1h$ one-body density matrix elements (OBDME's). For positive parity transitions, only $0\hbar\omega$ $1p$-$1h$ p-shell transitions were considered. The Millener and Kurath [50] (MK) interaction was used to calculate the OBDME's. These OBDME's are almost identical to the values reported by Lee and Kurath [51], which are derived from the Cohen-Kurath [CK(POT)] interaction. For negative parity transitions, we used OBDME's from a recent shell-model calculation reported by Warburton and Brown [52]. This calculation was done in a $1\hbar\omega$ $spsdpf$ model space, including $0s \to 0p$ and $0p \to 1s0d$ transitions. The interaction used by Warburton and Brown [52] for this shell-model calculation is the WBT interaction [52], which was obtained by least-squares fits to 51 $0p$-shell and 165 cross-shell binding energies. Also, the WBT interaction is constructed in a $0p1s0d$ shell-model space and the perturbative effects of neighboring $0s$ and $0f1p$ shells are considered. We also did some shell-model calculations for negative parity transitions using the MK interaction [50]. Results for the calculated differential cross-section angular distribution for the low-lying dipole states in the $^{12}C(p,n)^{12}N$ reaction using either the WBT or MK interactions are very similar. The OBDME's for 147 dipole states up to 40 MeV excitation energy obtained using the WBT interaction were used in the present study for the DWIA calculations.

Harmonic oscillator (HO) wave functions were assumed for the single particle states. For DWIA calculations the center-of-mass corrections are important because ^{12}C is

a light nucleus. These corrections have been made as described by Millener in the Appendix of Ref. [9]. A reduced HO size parameter $b_r = [\frac{A}{(A-1)}]^{1/2} b_0$ was used with an $(A-1)$ nucleus core mass . Values for the HO size parameter b_0 were obtained from the analysis of transverse electron scattering for each individual transition in ^{12}C [53–55]. For some of the transitions at higher excitation energy, there are no electron scattering results. In such cases we used the value $b_0 = 1.64$ fm which is the average value of all analyzed transitions in electron scattering from ^{12}C.

The distorted waves for incident and outgoing nucleons were calculated using optical-model potential (OMP) parameters obtained by Comfort and Karp [54] in the analysis of $20-200$ MeV proton elastic scattering data from ^{12}C. The energy dependence of the OMP parameters has been taken into account as suggested in Ref. [54]. Because these OMP parameters were obtained in the analysis of proton elastic scattering from ^{12}C $(T = 0)$, an asymmetry potential of $24.0(N - Z)/A$ MeV was included in the OMP for the outgoing channel. A Coulomb correction [56] term was also used to adjust the potential for the incoming or outgoing neutron.

B. Quasifree scattering

At energies above 150 MeV the quasifree contributions to the measured angular distributions need to be considered [24]. The data obtained for the ^{12}C$(p, n)^{12}$N reaction are quite suitable for a detailed analysis of the QF because they extend to an energy loss $\omega = 100$ MeV and to a momentum transfer $q = 2.5$ fm^{-1}. A more detailed analysis of quasifree scattering from p-shell nuclei in the (p, n) reactions at $E_p = 186$ MeV is given in Ref. [57]. Here we present a semiphenomenological quasifree analysis following the empirical peak fitting procedure developed by Erell *et al.* [25] in a study of pion charge-exchange reactions. The same procedure has been used by Raywood *et al.* [26]. The approach is to fit the QF peak with a predetermined Lorentzian shape with an exponential cutoff that simulates Pauli blocking on the low excitation energy side.

The double differential cross section is written [25] as a function of excitation energy E ,

$$\frac{\partial^2 \sigma}{\partial E \partial \Omega} = \begin{cases} N \frac{1-\exp[-(E-E_0)/T_p]}{1+[(E-E_{\mathrm{qf}})/W_L]^2}, & E > E_0 , \\ 0, & E \leq E_0 , \end{cases} \quad (4.1)$$

where N, E_0, T_p, E_{qf}, and W_L are parameters. For the ^{12}C$(p, n)^{12}$N reaction, the cutoff energy E_0 is the separation energy of the least bound proton in ^{12}N, i.e., 1.95 MeV. For the ^{12}C$(n, p)^{12}$B reaction, E_0 is 4.95 MeV. The value E_{qf} corresponds to the excitation energy (MeV) for the QF peak position. Empirical values are used for this quantity at angles $\theta_{\mathrm{lab}} \geq 15°$, where the QF peak is well separated from lower transitions. An empirical quadratic equation relating the energy loss ω and momentum transfer q for the QF peak location obtained for $15° \leq \theta_{\mathrm{lab}} \leq 50°$ was used to extrapolate to angles below $\theta_{\mathrm{lab}} < 15°$. The parameter N in Eq. (4.1) is associated with the effective number of nucleons inside the nucleus that participate in the QF process and is momentum transfer dependent. In the fitting we allow N to vary with angle as done in Ref. [26]. The value W_L represents the width of the Lorentzian peak and is directly related to the Fermi momentum of the nucleon that participates in the QF reaction, and it is expressed as

$$W_L = W_{L0} \left[1 + \alpha \left(\frac{q}{k_F} \right)^2 \right] , \quad (4.2)$$

where q is momentum transfer at E_{qf}, k_F is the Fermi momentum (297 MeV/c), and W_{L0} and α are adjustable parameters. The parameter T_p in Eq. (4.1) simulates the influence of Pauli blocking effects in the QF region. It has been suggested in Refs. [25, 26] to keep T_p constant. Here we obtain a better result by assuming that T_p has a similar q^2 linear relationship as in Eq. (4.2).

The ^{12}C$(p, n)^{12}$N spectra at each measured angle were fitted with a number of Gaussian peaks of proper widths and skewness for the low-lying discrete peaks and with a broad peak corresponding to the QF scattering at higher energy loss. The fitting results for the ^{12}C$(p, n)^{12}$N reaction at $E_p = 186$ MeV at $\theta_{\mathrm{lab}} = 5°$ and $25°$ are shown in Fig. 1.

The same QF fitting procedure as described above was performed for the ^{12}C$(n, p)^{12}$B reaction at energies above 150 MeV. For energies below 150 MeV, the continuum below the giant resonances was assumed to be mainly from multistep scattering rather than QF scattering. The fitting results are shown in Fig. 2.

The peak positions of the low-lying states were determined by empirical results and shell-model predictions (Fig. 3). Since the energy resolution of the present ^{12}C$(p, n)^{12}$N reaction is better than that of the ^{12}C$(n, p)^{12}$B reaction, we observe more structure in the low excitation energy region in the ^{12}C$(p, n)^{12}$N spectra (Figs. 1 and 2). We used seven Gaussian peaks to fit the ^{12}C$(p, n)^{12}$N spectra and four Gaussian peaks to fit the ^{12}C$(n, p)^{12}$B spectra up to 12 MeV excitation energy. The excitation energies and widths (FWHM) which were used for the Gaussian peaks are listed in Table I. The peak width and the peak position were fixed in the fitting procedure.

In Sec. IV C we present the results obtained with this peak fitting procedure for low-lying states in ^{12}N or ^{12}B, respectively. A complete discussion from the analysis of the QF scattering is reported in Ref. [57].

C. Low-lying states in ^{12}N and ^{12}B

1. The g.s., 2_1^+ and 2_1^- excited states

Due to the limited energy resolution obtained in the ^{12}C$(p, n)^{12}$N and ^{12}C$(n, p)^{12}$B reactions, three states [27] (Fig. 3) may contribute to the cross section observed for the first neutron and proton groups, respectively. These are the ground-state (1^+) transition, the 2_1^+ (0.96 MeV) and the 2_1^- (1.19 MeV) transitions in ^{12}N for the first neutron group (Fig. 1) and the ground-state (1^+) tran-

T=1 States
A=12 Isobar Diagram

^{12}B

E_x	J^π
10.0	
9.43	
9.04	1-
8.58	
8.10	
7.94	1-
7.84	1-
7.55	1-
7.06	1-
6.60	1+
5.73	3-
5.61	3-
5.00	1+
4.52	4-
4.38	
4.30	1-
3.76	2+
3.38	3-
2.72	0+
2.62	1-
1.67	2-
0.95	2+
[15.21]	1+

^{12}C (0+1)$\hbar\omega$ Calculation Ref.[52]

E_x	J^π
9.97	1-
9.77	2-
9.08	0-
8.99	2-
8.82	2-
8.77	1-
8.64	
8.51	2-
8.18	2-
8.11	
7.88	0+
7.76	1-
7.34	2+
7.06 7.08	1+ 2-
6.70	1-
6.31	2-
6.28	1-
6.18	2-
6.12	3+
4.59	1+
4.03	0-
3.88	
3.85	
3.79	2- 4-
3.50	2-
2.68	0+
2.32	1-
1.65	2-
0.86	2+
[15.11]	1+

^{12}N

E_x	J^π
10.30	
9.80	
9.04	
8.45	
7.68	1-
6.40	1-
5.60	
5.35	3-
4.14	2-,4-
3.56	1+
3.13	2+
2.44	0+
1.80	1-
1.19	2-
0.96	2+
[14.98]	1+

FIG. 3. $T = 1$ energy level diagram for $A = 12$. The experimental information for ^{12}B and ^{12}N nuclei were obtained from Ref. [27]. The $T = 1$ eigenstates from a shell-model calculation [52] for ^{12}C are shown in the middle column.

sition, the 2_1^+ (0.95 MeV) and 2_1^- (1.67 MeV) transitions in ^{12}B for the first proton group (Fig. 2). However, the shapes of the angular distributions for these three transitions are quite different, allowing them to be distinguished (see Fig. 4). To compare the data at slightly different incident energies, we plot the differential cross section (mb/sr) versus momentum transfer q (fm^{-1}) for these transitions. We present in Fig. 4 the center-of-mass differential cross section for the first neutron group measured in the ^{12}C$(p,n)^{12}$N reaction at E_p = 186 MeV (solid circles) and the center-of-mass differential cross section for the first proton group measured in the ^{12}C$(n,p)^{12}$B reaction at E_n =190 MeV (solid triangles). We have also included the forward angle data for the ^{12}C$(n,p)^{12}$B reaction reported by Sorenson et al. [37], that were also measured at LAMPF/WNR (solid squares). An excellent agreement is observed between the data sets, as expected for cross sections to isobaric states in self-conjugate nuclei.

The curves in Fig. 4 are DWIA calculations at E_p = 186 MeV, representing a Gamow-Teller (GT) transition (solid curve), an electric quadrupole ($E2$) transition (dashed curve), and a magnetic quadrupole ($M2$) transition (dot-dashed curve). While calculations for the $E2$ and $M2$ transitions required normalization factors of 0.4 and 0.7, respectively, no normalization was needed for the GT transition. Values for the HO size parameter $b_0 = 1.87$ fm (GT transition), $b_0 = 1.58$ fm ($E2$ transition), and $b_0 = 1.68$ fm ($M2$ transition) were used in the DWIA calculations. These values are from Refs. [54,55]. Incoherent sum of all these calculations agree quite well with the measured cross section up to a large momentum transfer ($q \sim 2.5$ fm^{-1}) (Fig. 4).

The spin observables measured in this experiment for the first neutron group in the ^{12}C$(\vec{p},\vec{n})^{12}$N reaction are shown in Fig. 5. Values for A_Y, P, and D_{NN} were measured at five angles up to momentum transfer $q = 1.25$ fm^{-1} (solid circles). Comfort et al. [30] reported A_Y values obtained in the ^{12}C$(\vec{p},\vec{p}')$ reaction at 200 MeV for the analog transitions. The A_Y values in Ref. [30] which are values for individual transitions, were weighted by the corresponding differential cross section to make the comparison with the present ^{12}C$(\vec{p},\vec{n})$ results. The data from Ref. [30] are shown with solid square symbols in Fig. 5. The D_{NN} value at 0° (cross) in Fig. 5 was mea-

TABLE I. Excitation energies and widths of the Gaussian peaks shown in Figs. 1 and 2. Γ: Peak width (FWHM) used to fit the spectra.

^{12}C$(p,n)^{12}$N		^{12}C$(n,p)^{12}$B	
E_x (MeV)	Γ (MeV)	E_x (MeV)	Γ^a (MeV)
0.00	1.0	0.00	2.5
0.96	1.0	4.89	2.5
2.40	1.1	8.11	2.8
4.50	1.5	12.4	3.2
6.40	2.0		
9.80	2.1		
11.5	2.1		

^{a} The FWHM listed here are values for E_n =160 – 180 MeV. For lower incident neutron energies, the corresponding values are smaller.

^{12}C(p,n)^{12}N; ^{12}C(n,p)^{12}B (g.s., 2_1^+, 2_1^-)
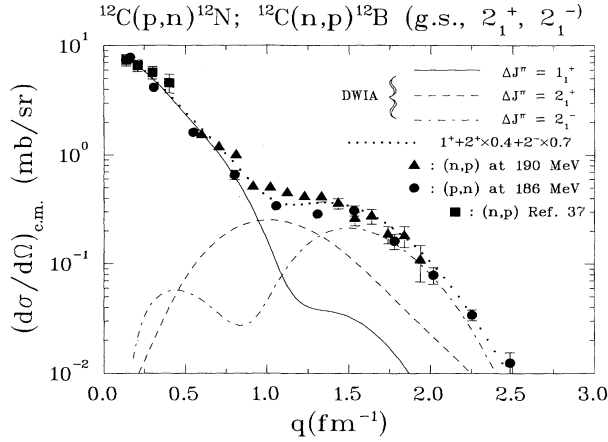
FIG. 4. Angular distributions of the differential cross section for g.s., 2_1^+ and 2_1^- transitions in the ^{12}C(p, n)^{12}N reaction at $E_p = 186$ MeV (solid circles) and in the ^{12}C(n, p)^{12}B reaction at $E_n=190$ MeV (solid triangles and solid squares). The curves are the DWIA calculations at $E_p = 186$ MeV.

sured by Taddeucci et al. [58] for the ^{12}C($\vec{p}, \vec{n}$)^{12}N(g.s.) transition at 160 MeV.

The solid curves in Fig. 5 are DWIA calculations obtained using the weighing factors for individual transitions indicated in Fig. 4. A good agreement is observed between the DWIA calculations and data except for the A_Y values. The discrepancy in A_Y between experimental results and DWIA calculations was also found by Comfort et al. in the ^{12}C($\vec{p}, \vec{p}'$) analysis [30]. In Ref. [30] it is noted that if in the transition density to the $T = 1, J^\pi = 1^+$ (15.11 MeV) state (characterized by orbital angular momentum, spin, and total angular momentum transfer $[LSJ]$[51]), the abnormal-parity spectroscopic amplitude $[LSJ] = [111]$ is removed, the A_Y results are improved considerably. However, other results do not totally support eliminating this amplitude. In particular $(P - A)$ measurements for the same tran-

sition at 150 MeV reported by Carey et al. [59] indicate that this amplitude is important. Similar results were reported for some other transitions in ^{12}C, such as the transitions to the $T = 0, J^\pi = 2^+$ (15.30 MeV) state and to the $T = 1, J^\pi = 2^+$ (16.11 MeV) state [30]. At this time we do not know the exact reason for the observed discrepancy in A_Y and P, since the calculated values for A_Y and P are sensitive to both nuclear structure and effective interaction. We have done DWIA calculations with the [111] amplitude removed for the g.s. transition. The results including the unmodified calculations for the $E2$ and $M2$ transitions are presented in Fig. 5 (dashed line). A much better agreement is observed for the calculated values of A_Y and P.

2. States around 4 MeV

Several states (see Fig. 3) are excited [27] in ^{12}B and ^{12}N near 4.5 MeV in the ^{12}C(n, p)^{12}B and ^{12}C(p, n)^{12}N reactions [9, 13]. Principally two states contribute to the observed charge-exchange cross section. They have been identified as a negative parity doublet with $J^\pi = 2_2^-$ and $J^\pi = 4_1^-$. In the present experiment we are able to differentiate their contributions in the measured angular distribution. As shown in Fig. 6, the 2_2^- state is stronger at lower momentum transfer region (or forward angles), while the 4_1^- state is strongly excited at higher momentum transfers. Because of the limitation of the energy resolution in the present experiment, the strong peak centered at 4.5 MeV in the energy spectra may possibly have contributions from other several neighboring states, for example, in ^{12}B, the 1_2^+ (5.0 MeV) state and the 1_2^- (4.3 MeV) state [27] (Fig. 3). Based on DWIA calculations we present in Fig. 6 the four strongest transitions in the 4.5-MeV excitation energy region. These results show a good agreement with the ^{12}C(p, n)^{12}N and ^{12}C(n, p)^{12}B data which have the QF contributions subtracted.

If the nuclear structure calculation is constrained to 1
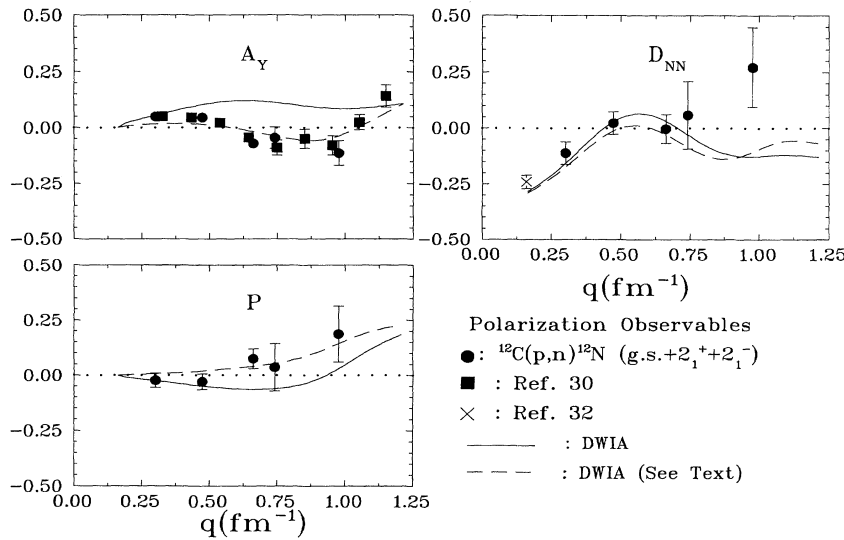
FIG. 5. Spin observables for the transitions indicated in Fig. 4 are presented vs momentum transfer q for the ^{12}C($\vec{p}, \vec{n}$)^{12}N reaction at $E_{\vec{p}} = 160$ and 186 MeV. The curves are the DWIA calculations for $E_{\vec{p}} = 186$ MeV.

Polarization Observables
● : ^{12}C(p,n)^{12}N (g.s.+2_1^++2_1^-)
■ : Ref. 30
✕ : Ref. 32
——— : DWIA
– – – : DWIA (See Text)

^{12}C(p,n)^{12}N; ^{12}C(n,p)^{12}B (E$_x \approx$ 4.5 MeV)
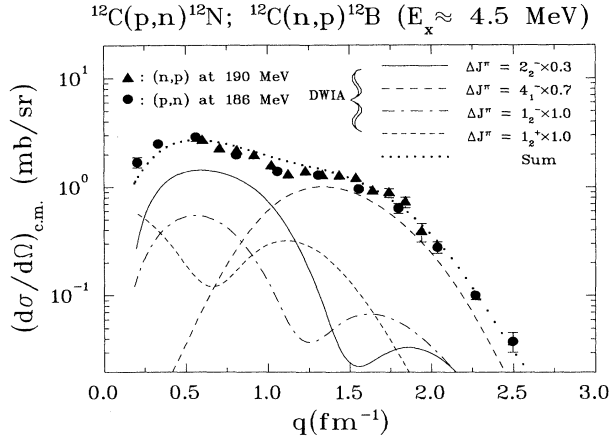
FIG. 6. Angular distributions of the differential cross sections for the transitions around 4.5 MeV excitation in the ^{12}C$(p,n)^{12}$N reaction at E_p = 186 MeV (solid circles) and in the ^{12}C$(n,p)^{12}$B reaction at E_n = 190 MeV (solid triangles)

$\hbar\omega$ shell-model space and HO wave functions are used [9], as done in this work, usually normalization factors are required for both the $M2$ and the $M4$ transitions. Of course, the normalization factors depend on the values of the HO size parameter b_0 used in the DWIA calculations. In the present study we use the value b_0 = 1.52 fm for the 4_1^- state and b_0 =1.64 fm for the other three transitions [30, 53, 55]. The obtained normalization factors are 0.3 and 0.7 for the 2_2^- and 4_1^- contributions, respectively.

The DWIA calculations for the 2_2^- transition, underestimate the data at forward angles. This is a problem that has been noted in other cases for spin-dipole transitions, such as the ^{40}Ca$(p,n)^{40}$Sc (2_1^-) transition reported by Taddeucci et al. [60] and in the ^{15}N$(n,p)^{15}$C reaction reported by Celler et al. [61]. It is possible that because of the present resolution the transitions to 1_2^+ (5.0 MeV) and 1_2^- (4.3 MeV) contribute to the measured cross section. We have included these transitions as shown in Fig.

6, and although the agreement with the measured cross section is not as good as that in Fig. 4, it is reasonable. A similar problem in reproducing the transition to the 2_2^- state is reported by Gaarde et al. [13] and Olsson et al. [12]. The fact that with DWIA calculations we cannot reproduce exactly the shape of empirical angular distributions in transitions characterized with a ΔJ^π = 2^- introduces an additional uncertainty in the multipole decomposition analysis and as such MDA results should be interpreted cautiously.

The spin observables for the neutron group at 4.5 MeV measured in the ^{12}C$(\vec{p}, \vec{n})^{12}$N reaction are presented in Fig. 7. Almost all the observables are well reproduced by the DWIA calculations which include the four transitions as indicated in Fig. 6. The weighing factors shown in Fig. 6 have been used in the calculations of the spin observables by summing incoherently all the transitions involved (solid curve).

3. States around 7 MeV

In Fig. 8, the data points are differential cross sections obtained for the third peak shown in the energy spectra (Figs. 1 and 2). The cross sections were obtained by integrating the total number of counts between 6.0 MeV and 9.5 MeV of excitation energy after the QF contributions were subtracted. Again the results obtained in ^{12}C$(p, n)^{12}$N and ^{12}C$(n, p)^{12}$B data agree well with each other. The energy levels diagrams of A = 12 nuclei (Fig. 3) [27] indicate that there are several states around 7.0 MeV excitation in ^{12}N and ^{12}B. Based on the shell-model calculations (Sec. IV A), five 1^- states, six 2^- states, two 0^- states, one 1^+ state, one 2^+ state, and one 3^+ state are located in the above excitation energy region. The solid, dashed, and dot-dashed curves in Fig. 8 are DWIA calculations (b_0=1.64 fm) for the sum of the transitions to the five 1^- states, the six 2^- states, and the two 0^- states and to the three positive parity states, respectively. At lower momentum transfers the $E1$ DWIA calculations
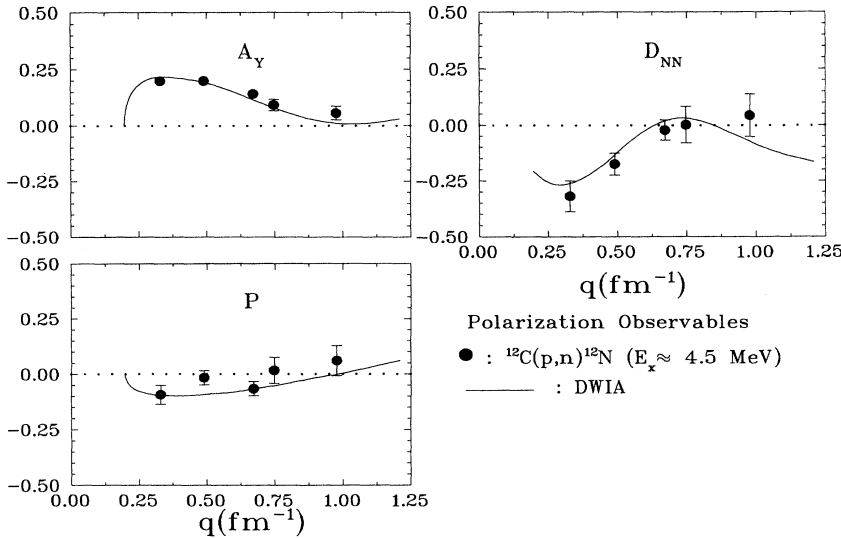
FIG. 7. Spin observables for the transitions indicated in Fig. 6 are presented vs momentum transfer q for the ^{12}C$(\vec{p}, \vec{n})^{12}$N reaction at $E_{\vec{p}}$ = 160 and 186 MeV.

^{12}C(p,n)^{12}N; ^{12}C(n,p)^{12}B (E$_x$ $\approx$ 6.0–9.5 MeV)
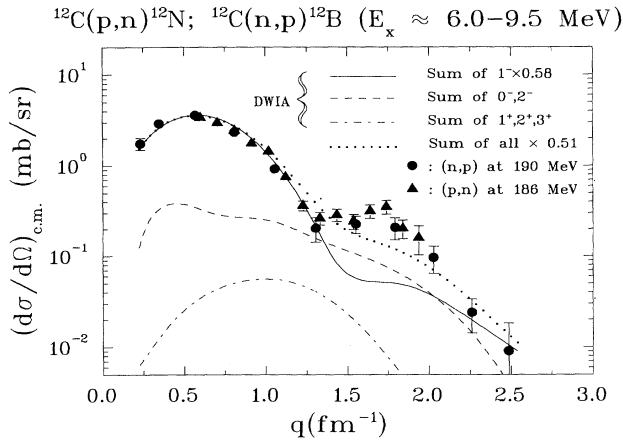
FIG. 8. Angular distributions of the differential cross sections for transitions around 7.5 MeV excitation in the ^{12}C(p,n)^{12}N reaction at E_p = 186 MeV (solid circles) and in the ^{12}C(n,p)^{12}B reaction at E_n = 190 MeV (solid triangles)

with a normalization factor of 0.58 fit the data quite well. The sum of all these 16 transitions is shown as a dotted curve in Fig. 8 with a normalization factor of 0.51. It underpredicts the differential cross section around the momentum transfer $q \sim 1.7$ fm^{-1}. One possible explanation for this is that higher multipolarity states which are not included in our calculation, may contribute to the differential cross section in this region.

The polarization observables obtained in the ^{12}C($\vec{p}, \vec{n}$)^{12}N reaction for the neutron group between 6 and 9.5 MeV excitation are presented in Fig. 9. A fair agreement is obtained between the DWIA calculations and data for A_Y. However, values for P and D_{NN} are not well reproduced.
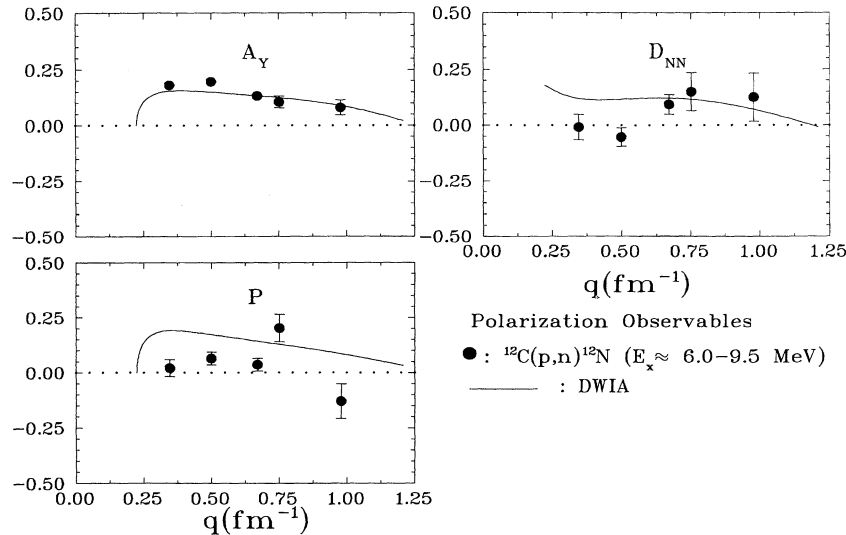
D. Multipole decomposition analysis (MDA)

To extract further information from the data, we employed a multipole decomposition analysis (MDA) [33, 34] to get the distribution in excitation energy for transitions with different ΔL transfers. For the ^{12}C(p, n)^{12}N reaction data at 186 MeV, the double differential cross sections were binned in 0.5-MeV intervals for the angles between θ_{lab} = 0° and 25°, and converted into center-of-mass double differential cross sections assuming two-body kinematics. Then the data were fitted with a weighted summation of DWIA outputs with different ΔJ^π transfers. Similar MDA procedures were applied to the ^{12}C(n, p)^{12}B data at E_n = 180–200 MeV and E_n =90–100 MeV, except that a larger energy bin size (0.8 MeV) was used. We have calculated the angular distribution for $1p$-$1h$ configurations with final J^π states 0^-, 1^+,1^-, 2^+, 2^-, 3^+, 3^-, and 4^-. The shapes of angular distributions are characterized by ΔJ^π transfers. Based on the shell-model calculations which are described in Sec. IV A, we have performed DWIA calculations by choosing $1p$-$1h$ configurations with the largest amplitude to represent each ΔJ^π transition in the MDA. Since the shape of $\sigma(\theta)$ changes smoothly with increasing excitation energy E_x, we have done DWIA calculations in 5-MeV excitation energy intervals between 0 and 30 MeV for each $1p$-$1h$ configuration. An interpolation routine [34] was used to obtain the necessary shapes in steps of 0.5 MeV. Since the differences in shape for spin-flip and non-spin-flip transitions with the same ΔL are not large enough to distinguish them [33], we present the final MDA results by grouping all ΔJ^π transitions corresponding to a given ΔL transfers. For instance, ΔJ^π = 1^+ transitions are assigned to ΔL = 0 while ΔJ^π = 0^-, 1^-, 2^- are assigned to ΔL =1.

In the present study the transitions characterized with ΔL =0, 1, and 2 are our main interests. The MDA results have been obtained for angles between θ_{lab} = 0° and 25°.

Some of the results obtained at θ_{lab} = 10° for both

FIG. 9. Spin observables for the transitions indicated in Fig. 8 are presented vs momentum transfer q for the ^{12}C($\vec{p}, \vec{n}$)^{12}N reaction at $E_{\vec{p}}$ = 160 and 186 MeV.

Polarization Observables

● : ^{12}C(p,n)^{12}N (E$_x$ $\approx$ 6.0–9.5 MeV)

——— : DWIA
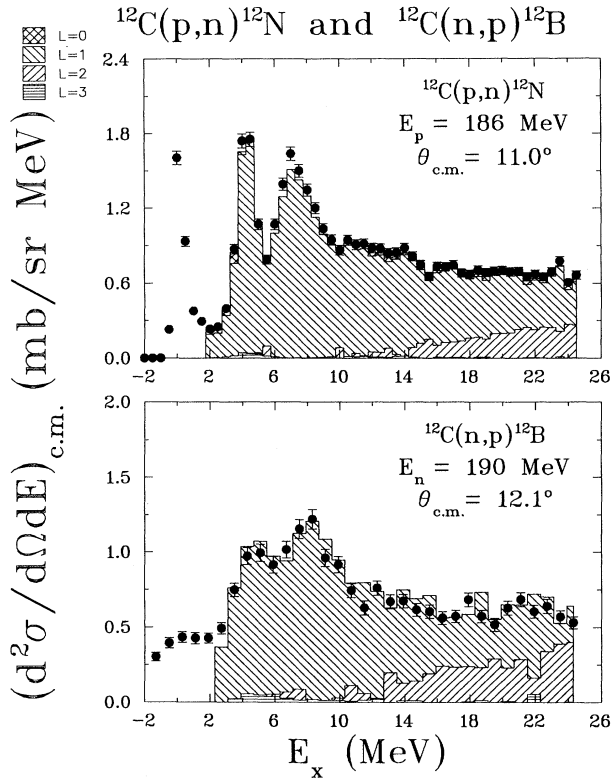
FIG. 10. The multipole decomposition analyzed $^{12}C(p,n)^{12}N$ data at $E_p = 186$ MeV and $\theta_{c.m.} = 11°$ and the $^{12}C(n,p)^{12}B$ data at $E_n=190$ MeV and $\theta_{c.m.} = 12°$.

$^{12}C(p,n)^{12}N$ and $^{12}C(n,p)^{12}B$ are shown in Fig. 10. A large strength of $\Delta L = 1$ transitions shows up centered at 4 and 7 MeV excitation energies.

E. Dipole ($L = 1, \Delta S = 0$) and spin-dipole ($L = 1, \Delta S = 1$) resonances

The energy spectra of the $^{12}C(p,n)^{12}N$ and $^{12}C(n,p)^{12}B$ charge-exchange reactions (Figs. 1 and 2) show strong transitions characterized with $\Delta L = 1$ at $\theta_{lab} \sim 10°$, which corresponds to $q \sim 0.5$ fm^{-1}, where the angular distribution reaches the maximum for the $\Delta L = 1$ transitions. This is emphasized in the MDA results shown in Fig. 10. At low incident energies (50 $\leq E \leq$100 MeV) charge-exchange reactions preferentially excite spin-independent transitions because of the dominance of the isospin spin-independent (τ) interaction over the spin isospin ($\sigma\tau$) interaction [1,2]. However at higher incident energies (150 $\leq E \leq$ 300 MeV) spin transitions and in particular the giant spin dipole resonance (GSDR) are strongly excited [1,2]. In this section, we discuss the energy dependence of the GDR and GSDR measured in the $^{12}C(n,p)^{12}B$ reaction with the continuous neutron energy source between 60 and 260 MeV. We also present DWIA calculations for $\Delta L = 1$ ($\Delta J^\pi = 0^-, 1^-, 2^-$) transitions to 147 states as described in Sec. IV A which are compared with the MDA results and RPA-DWIA calculations.

1. Energy dependence of GDR and GSDR

The $\Delta J^\pi = 1^-$ transitions to the residual nuclei, ^{12}N or ^{12}B, may possibly have both spin-transfer ($\Delta S = 1$) and non-spin-transfer ($\Delta S = 0$) contributions. It is difficult to extract information of the amount of spin strength and nonspin strength observed in $\Delta J^\pi = 1^-$ transitions, just from differential cross-section data. However the study of the energy dependence of giant dipole resonances allows us to distinguish the spin-flip (GSDR) and non-spin-flip (GDR) transitions (see Ref. [34]). As indicated in Sec. I, one would expect that in the charge-exchange reaction the GDR is dominant at incident energy below 100 MeV and decreases with increasing incident energy while the GSDR is dominant at incident energy above about 150 MeV. We choose the analyzed data at $E_n = 70-80$ MeV and at $E_p = 186$ MeV to do the comparison.

In order to empirically observe the energy dependence of the dipole and the spin-dipole resonances, a 3D plot ($E_x, E_n, d^2\sigma/d\Omega dE$) of the $^{12}C(n,p)^{12}B$ data at a momentum transfer $q \sim 0.7$ fm^{-1} has been made to show how the measured differential cross section changes with incident neutron energy. In Fig. 11 one can clearly see two resonances centered at 4.5 MeV and 7.0 MeV. These two resonances have mixed spin-flip and non-spin-flip transitions, but a stronger increase in cross section with energy is noted for the transitions at $E_x \sim 4.5$ MeV (2^-) than that for the transitions at $E_x \sim 7.0$ MeV (1^-).

We also have done MDA for two other sets of data for the $^{12}C(n,p)^{12}B$ reaction at energies $E_n =90-100$ MeV and $E_n =60-70$ MeV. The obtained results at $E_n=60-70$ MeV agree very well with the results reported at 60 and 65 MeV by Brady et al. [9] and are not presented here. Olsson et al. [12] have recently published an analysis of the $^{12}C(n,p)^{12}B$ at 98 MeV. Again, the present results at $E_n = 90-100$ MeV agree very well with the data from Ref. [12] and are not presented here.

Back-angle electron scattering is a useful probe to select isovector magnetic transitions. The GSDR was studied by Hicks et al. [53] with the $^{12}C(e,e')^{12}C$ reaction at 196.5 MeV. We compare the spectrum of the present $^{12}C(p,n)^{12}N$ reaction at $E_p= 186$ MeV and $\theta_{lab} = 10°$ with the above $^{12}C(e,e')^{12}C$ spectrum. This qualitative
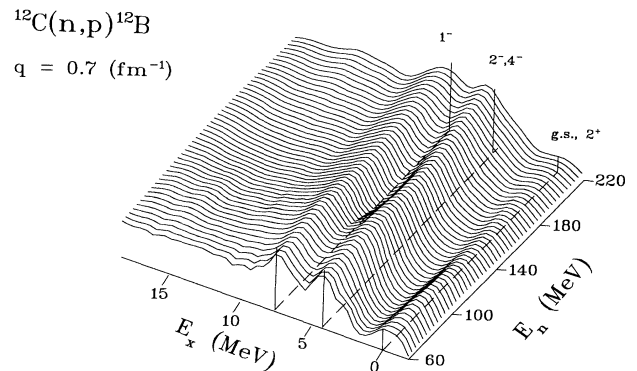
FIG. 11. 3D plot ($E_x, E_n, d^2\sigma/d\Omega dE$) for the $^{12}C(n,p)^{12}B$ reaction with incident neutron energies from 60 to 260 MeV at a momentum transfer $q \sim 0.7$ fm^{-1}.

GSDR and GDR
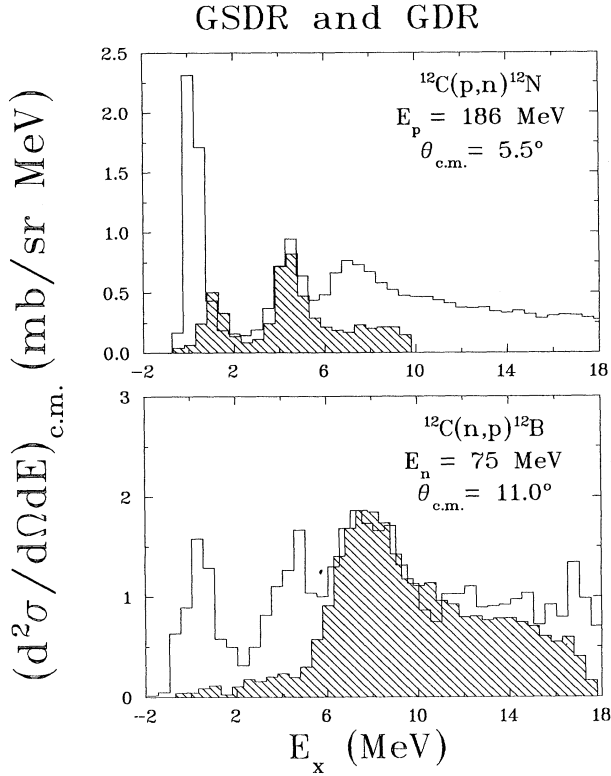
FIG. 12. Top: comparison of energy spectra for the $^{12}C(p,n)^{12}N$ reaction at $\theta_{c.m.} = 5.5°$ and $E_p = 186$ MeV and the GSDR results (shaded area) obtained in back-angle electron scattering at 196.5 MeV [53]. Bottom: comparison of energy spectra for the $^{12}C(n,p)^{12}N$ reaction at $\theta_{c.m.} = 11°$ and $E_n = 75$ MeV and the GDR results (shaded area) obtained in the $^{12}C(\gamma,n)^{11}C$ reaction [17] (bottom).

comparison in the top half of the Fig. 12, is just to show the shape and the location of the GSDR. The shaded area represents the spectrum of the $^{12}C(e,e')^{12}C$ reaction which have been shifted about -15 MeV because of the Q values and arbitrarily normalized to the $^{12}C(p,n)^{12}N$ spectrum. The comparison indicates that spin transitions are the major contributions in the peak centered at 4.5 MeV. The peak centered at 7 MeV in the $^{12}C(e,e')^{12}C$ spectrum shows a relatively small amount of spin transition strength.

The photonuclear $^{12}C(\gamma,n)^{11}C$ reaction [17] is a unique probe to excite the GDR. The energy spectrum from the $^{12}C(\gamma,n)^{11}C$ reaction is compared with that of the $^{12}C(n,p)^{12}B$ reaction at $\theta_{lab} = 11°$ with $E_n = 70-80$ MeV and displayed in the bottom half of Fig. 12. The

shaded area is the arbitrarily normalized spectrum from the $^{12}C(\gamma,n)^{11}C$ reaction which has been shifted about -15 MeV. The GDR is mainly excited in the range between 6.0 and 9.5 MeV excitation. The peak centered at 4.5 MeV has very small contributions from non-spin-transfer transitions. This is consistent with the above discussions.

2. RPA-DWIA calculations

The nuclear structure information for DWIA calculations in the previous sections in this paper were based on a conventional shell model in which only the one-body interaction characterized as a Hartree-Fock (*mean-field*) Hamiltonian has been considered. The excitations are interpreted as different particle-hole configurations in a constrained finite shell-model space. Giant resonances can be described in terms of collective oscillation of nucleons in nuclei. In such a system which involves a many-body motion, the residual interactions and the ground-state correlations have to be taken into account. In this section we present a random phase approximation (RPA) analysis for the $^{12}C(p,n)^{12}N$ reaction at 186 MeV, which includes the above considerations.

The microscopic RPA-DWIA calculation was implemented in two steps. First, the nuclear structure information was obtained from RPA calculations [62-65], in which the excited states are treated as a coherent sum of particle-hole excitations. The single particle states are determined by a Woods-Saxon potential with chosen parameters to reproduce the experimental binding energies and single-particle spectrum near the Fermi surface. These parameters are listed in Table II [66]. The single particle states have been expanded in terms of HO wave functions with an oscillator parameter length of $b_0 = 1.67$ fm. Thus a discretized continuum was obtained. A Landau-Migdal force [67-69] was used as the residual interaction:

$$V_{res}(\mathbf{r}, \mathbf{r}') = C_0\delta(\mathbf{r} - \mathbf{r}')[f_0' + g_0'\boldsymbol{\sigma} \cdot \boldsymbol{\sigma}']\boldsymbol{\tau} \cdot \boldsymbol{\tau}', \quad (4.3)$$

where $C_0 = 300$ MeV fm^3, $f_0' = 1.5$, and $g_0' = 1.0$. Transition densities obtained from this RPA calculation, folded with the effective interaction give form factors as a starting point for distorted wave calculations. The effective projectile-target interaction was described by the free t matrix of Franey and Love [48].

The same optical model potential parameters described in Sec. IV A have been used to calculate the distorted waves. The DWIA calculations have been performed with a computer code based on DWUCK4 [70]. We have calculated transitions with nine different multipo-

TABLE II. Woods-Saxon potential[a] parameters.

^{12}C	V_0(MeV)	R (fm)	a (fm)	V_{LS} (MeV)
p	-62.0	2.86	0.57	3.20
n	-60.0	2.86	0.57	3.15

[a] The optical model potential used was of the form $V(r) = V_0 f(X_i) + 4V_{LS} g(X_i) L \cdot S$, where $f(X_i) = [1 + \exp(X_i)]^{-1}$ and $g(X_i) = \frac{1}{r}\frac{d}{dr}\left(\frac{d[f(X_i)]}{dX_i}\right)$, $X_i = \left(\frac{r-R}{a}\right)$.

larities $(0^+, 1^+, 2^+, 3^+, 0^-, 1^-, 2^-, 3^-, 4^-)$ and for an excitation energy up to 50 MeV.

Basically, the $1p$-$1h$ excitations in the RPA calculation give strengths of the transitions and centroid of the excited states. A Breit-Wigner distribution, characterized by an energy dependent width Γ, due to the $2p$-$2h$ damping effects [71] was used to give appropriate descriptions for giant resonances in the continuum spectra. A detailed description of the RPA-DWIA formalism can be found in Refs. [72–74].

The RPA calculations are compared with the MDA results obtained in the $^{12}C(p,n)^{12}N$ reaction in Fig. 13. The data points are from the $^{12}C(p,n)^{12}N$ reaction at $E_p = 186$ MeV and at $\theta_{c.m.} = 5.5°$. A value $B_{th}(GT) = 1.334$ for the GT strength of $^{12}C(p,n)^{12}N$ (g.s.) transition was calculated in the RPA calculations. Since the empirical $B(GT)$ value [27] is 1.0, a normalization of 0.749 was assumed for the RPA-DWIA calculations for the $\Delta L = 0$ transitions. We also included a factor of 3.0 for the calculations of the $\Delta L = 1, 2,$ and 3 transitions to fit the data. To our knowledge, this is the first time that RPA-DWIA calculations have been reported for a light nucleus (^{12}C).

3. Energy distribution for $\Delta L = 1$ transitions in ^{12}N and ^{12}B

The top segment of Fig. 14 shows the energy distribution for $\Delta L = 1$ transitions obtained using a conven-
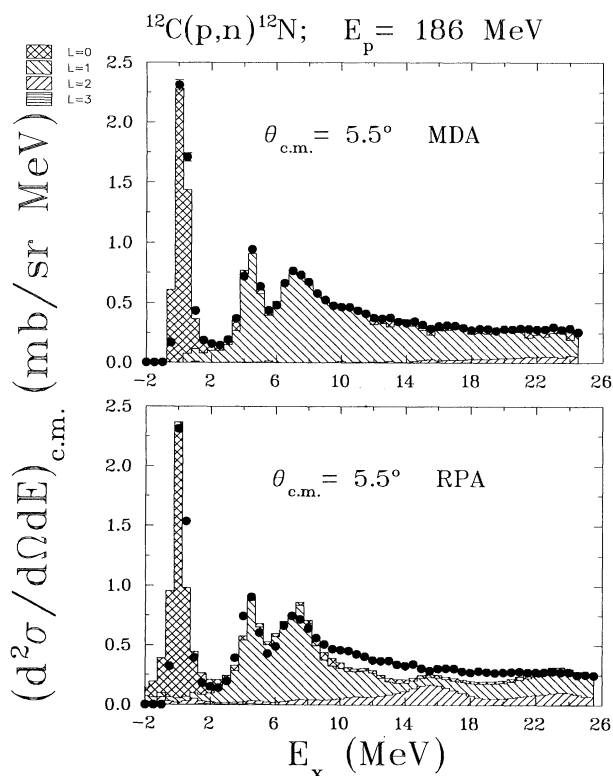
FIG. 13. Comparison of the results from MDA (top) and RPA-DWIA calculations (bottom) for the $^{12}C(p,n)^{12}N$ reaction at $E_p = 186$ MeV and $\theta_{c.m.} = 5.5°$.
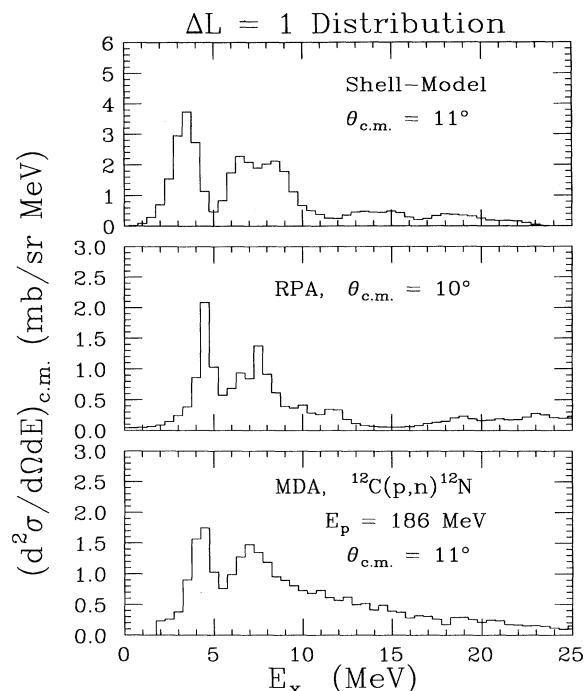
FIG. 14. $\Delta L = 1$ energy distribution for the $^{12}C(p,n)^{12}N$ reaction at $\theta_{c.m.} = 11°$ and $E_p = 186$ MeV. Results from DWIA calculations using $1p$-$1h$ transitions are presented in the top of this figure. Results from RPA-DWIA calculations are shown in the middle of this figure. The MDA results (Fig. 10 top) are displayed in the bottom of this figure.

tional $1p$-$1h$ shell model calculation [52] as indicated in Sec. IV A. This calculation indicates that there are 126 transitions with $\Delta L = 1$ transfer up to excitation energy of about 25 MeV. For each of these transitions, the DWIA cross section has been folded with a 1-MeV FWHM Gaussian distribution, to match the energy resolution of the experimental data. The $\Delta L = 1$ strength seems to be largely concentrated in two low-lying groups at about the observed excitation energy. However, the calculated differential cross sections are much larger (see Table III) than the experimental results [9, 13, 12]. In the middle segment of Fig. 14 we present the RPA-DWIA calculations for $\Delta L = 1$ transitions. In this calculation there are hundreds of $\Delta L = 1$ transitions up to 50 MeV excitation energy. Most of the strength however, seems to be concentrated at around 4 MeV and 7 MeV. The strength is much more fragmented than that obtained with the simple shell-model calculation. Compared with the experimental data, the RPA gives better predictions both in location and strength (see Table III) than the $1p$-$1h$ shell-model calculation.

A numerical evaluation of the integrated $\Delta L = 1$ strengths are presented in Table III. Values are given for the sum of the cross section in the 0−10-MeV excitation energy region and in the region between 0 and 25 MeV. The theoretical values are the summation of calculated cross-sections for $\Delta J^\pi = 0^-, 1^-, 2^-$ transitions in the same excitation energy region. The cross-section values are at a momentum transfer $q \sim 0.5$ fm^{-1}, which corre-

TABLE III.   Integrated $\Delta L = 1$ strength.

	[a]Exp. $\frac{d\sigma}{d\Omega}$ (mb/sr)	[b]DWIA (mb/sr)	[c]DWIA (mb/sr)
E_x (MeV)	[0−10]; [0−25]	[0−10]; [0−25]	[0−10]; [0−25]
^{12}C$(p,n)^{12}$N 186 MeV	8.13±0.18; 16.14±0.19	15.36; 19.85	10.17; 13.39
^{12}C$(n,p)^{12}$B 190 MeV	7.69±0.42; 14.54±0.75	15.36; 19.85	10.17; 13.39
^{12}C$(n,p)^{12}$B 95 MeV	8.34±0.29; 16.78±0.74	16.26; 20.42	10.17; 13.39

[a] The experimental values are MDA results. See Sec. IV D. Only statistical errors are included.
[b] DWIA calculation using the OBDME's from Ref. [52].
[c] RPA-DWIA calculation.

spond to a value $\theta_{\rm lab} \sim 10°$ at an incident energy $E_p \sim$190 MeV and $\theta_{\rm lab} \sim 14°$ at an incident energy $E_n \sim$100 MeV.

For the ^{12}C$(p,n)^{12}$N reaction at 186 MeV we observed about half of the $\Delta L = 1$ cross section predicted below 10 MeV of excitation by the shell-model calculations [52]. A similar value was obtained in the analysis of the ^{12}C$(n,p)^{12}$B reaction at 190 MeV. However, about 80% of the predicted cross section below 20 MeV excitation is excited in these reactions. Olsson et al. [12] reported that 70% of the $\Delta L = 1$ strength calculated using a similar shell model was observed in the ^{12}C$(n,p)^{12}$B reaction at 98 MeV in the excitation energy region below 30 MeV.

With residual interactions and ground-state correlations included, one would expect that the RPA calculations will give a more realistic prediction of the empirical strength. In Table III we present the DWIA-RPA results which indicate a better agreement between the empirical values and the theoretical predictions.

V. CONCLUSIONS

The ^{12}C$(p,n)^{12}$N reaction has been studied at E_p=186 MeV in the angular range $0° \leq \theta_{\rm lab} \leq 50°$. The ^{12}C$(n,p)^{12}$B reaction has been studied at E_n=60−260 MeV for the angles $11° \leq \theta_{\rm lab} \leq 37°$. The present experimental data covering a large angular range and up to a high energy loss ($\omega \sim 80$ MeV), have enabled us to quantitatively study the QF region using an empirical function as described in Sec. IV B. Assuming an incoherent process, the tail of the QF contributions in the giant resonance region was subtracted. Differential cross-section angular distributions for the low-lying transitions in the residual nuclei ^{12}N and ^{12}B show good agreement with

DWIA calculations in a large angular range (see Figs. 4, 6, and 8).

Spin observables A_Y, P, and D_{NN} for low-lying states, have been measured in the ^{12}C$(\vec{p}, \vec{n})^{12}$N reaction at five angles with polarized beam $E_{\vec{p}} = 160$ MeV and 186 MeV. Overall, a reasonable agreement is observed between the DWIA calculations and experimental data.

The energy dependence of the GDR and GSDR has been studied in the ^{12}C$(n,p)^{12}$B reactions (Fig. 11). The shapes and locations of the GDR and GSDR agree with the results of the ^{12}C$(\gamma, n)^{11}$C reaction and back-angle electron scattering data, respectively (Fig. 12).

It can be concluded from the present analysis that the DWIA calculations as described in Sec. IV A give good predictions of the differential cross-section angular distributions to discrete states (Figs. 10, 13, and 14). The MDA is a useful method to differentiate the different multipolarities in the giant resonance region. Of course the reliability of MDA depends mainly on reproducing empirical angular distribution shapes with DWIA calculation. The RPA-DWIA calculations indicate a satisfactory agreement with the MDA results. The $\Delta L = 1$ strength energy distribution of the ^{12}C$(p,n)^{12}$N reaction is well described by DWIA calculations using the recent shell-model calculations by Warburton and Brown [52], and by the RPA-DWIA calculations.

ACKNOWLEDGMENTS

[1] G.F. Bertsch and H. Esbensen, Rep. Prog. Phys. 50, 607 (1987).
[2] W.G. Love and M.A. Franey, Phys. Rev. C 24, 1073 (1981).
[3] D.J. Horen et al., Phys. Lett. 95B, 27 (1980).
[4] J. Rapaport et al., Phys. Rev. C 24, 335 (1981).
[5] C. Gaarde et al., Nucl. Phys. A396, 127c (1983).
[6] J. W. Watson et al., Phys. Rev. C 40, 22 (1989).
[7] J.N. Knudson et al., Phys. Rev. C 22, 1826 (1980).

[8] J. Mildenberger et al., Phys. Rev. C 42, 732 (1990).
[9] F.P. Brady et al., Phys. Rev. C 43, 2284 (1991).
[10] K.P. Jackson et al., Phys. Lett. B 201, 25 (1988).
[11] D.S. Sorenson et al., Phys. Rev. C 45, 500 (1992).
[12] N. Olsson et al., Uppsala University Neutron Physics report, 1992.
[13] C. Gaarde et al., Nucl. Phys. A422, 189 (1984).
[14] C. Gaarde et al., Nucl. Phys. A369, 258 (1981).
[15] F. Osterfeld, Phys. Lett. 105B, 257 (1981).

[16] K.C. So *et al.*, Nucl. Phys. **A517**, 473 (1990).

[17] J. Ahrens *et al.*, Nucl. Phys. **A251**, 479 (1975).

[18] W.A. Sterrenburg *et al.*, Nucl. Phys. **A405**, 109 (1983).

[19] T. Motobayashi *et al.*, Phys. Rev. C **34**, 2365 (1986).

[20] M. Moosburger *et al.*, Phys. Rev. C **41**, 2925 (1990).

[21] S. Nakayama *et al.*, Phys. Rev. C **46**, 1667 (1992).

[22] N. Anantaraman *et al.*, Phys. Rev. C **44**, 398 (1991).

[23] P.W. Lisowski *et al.*, Nucl. Sci. Eng. **106**, 208 (1990).

[24] C. Kalbach, Phys. Rev. C **41**, 1656 (1990).

[25] A. Erell *et al.*, Phys. Rev. C **34**, 1822 (1986).

[26] K.J. Raywood *et al.*, Phys. Rev. C **41**, 2836 (1990).

[27] F. Ajzenberg-Selove *et al.*, Nucl. Phys. **A433**, 100 (1985).

[28] S.J. Seestrom-Morris *et al.*, Phys. Rev. C **26**, 2131 (1982).

[29] J.B. McClelland *et al.*, Phys. Rev. Lett. **52**, 98 (1984).

[30] J.R. Comfort *et al.*, Phys. Rev. C **26**, 1800 (1982).

[31] J. Rapaport *et al.*, Phys. Rev. C **36**, 500 (1987).

[32] T.N. Taddeucci, Can. J. Phys. **65**, 557 (1987).

[33] M.A. Moinester, Can. J. Phys. **65**, 660 (1987).

[34] B.K. Park *et al.*, Phys. Rev. C **45**, 1791 (1992).

[35] C.D. Goodman *et al.*, IEEE Trans. Nucl. Sci. NS-26, 2248 (1979).

[36] T.N. Taddeucci *et al.*, Nucl. Instrum. Methods **A241**, 448 (1985).

[37] D.S. Sorenson, Ph.D. thesis, University of California, Davis, 1991.

[38] B.K. Park, Ph.D. thesis, Ohio University, 1991.

[39] A.G. Ling *et al.*, Phys. Rev. C **44**, 2794 (1991).

[40] L. Wang *et al.*, Phys. Rev. C **47**, 2123 (1993).

[41] R.S. Henderson *et al.*, Nucl. Instrum. Methods **A257**, 97 (1987).

[42] Arndt and L. D. Soper, Scattering Analysis Interactive Dial-in (SAID) program, (SP92) (unpublished).

[43] T.N. Taddeucci *et al.*, Nucl. Phys. **A469**, 125 (1987).

[44] T.N. Taddeucci *et al.*, Phys. Rev. C **41**, 2548 (1990).

[45] A.G. Ling, *Detector Calibration Procedures for (n, p) Experiment, at WNR/LAMPF*, 1990 (unpublished).

[46] Computer Code MAGPLT, developed by T. Ford, B. McEachern, and J.L. Romero, 1988 (unpublished).

[47] R. Schaeffer and J. Raynal, Program DWBA70 (unpublished); extended version DW81 by J.R. Comfort (unpublished).

[48] M.A. Franey and W.G. Love, Phys. Rev. C **31**, 488

[49] B.A. Brown *et al.*, The Oxford-Buenos Aires-MSU Shell-Model code OXBASH, Michigan State University Cyclotron Lab Report 524, 1986.

[50] D.J. Millener and D. Kurath, Nucl. Phys. **A255**, 315 (1975).

[51] T.-S.H. Lee and D. Kurath, Phys. Rev. C **21**, 293 (1980).

[52] E.K. Warburton and B.A. Brown, Phys. Rev. C **46**, 923 (1992).

[53] R.S. Hicks *et al.*, Phys. Rev. C **30**, 30 (1984).

[54] J.R. Comfort and B.C. Karp, Phys. Rev. C **21**, 2162 (1980).

[55] J.B. Flanz *et al.*, Phys. Rev. Lett. **41**, 1642 (1978); J.B. Flenz, Ph.D. thesis, University of Massachusetts, 1979.

[56] J. Rapaport, Phys. Rep. **87**, 25 (1982).

[57] L. Wang *et al.* (unpublished).

[58] T.N. Taddeucci *et al.*, Phys. Rev. Lett. **52**, 1960 (1984).

[59] T.A. Carey *et al.*, Phys. Rev. Lett. **49**, 266 (1982).

[60] T.N. Taddeucci *et al.*, Phys. Rev. C **28**, 2511 (1983).

[61] A. Celler *et al.*, Phys. Rev. C **43**, 639 (1991).

[62] D.J. Rowe, Nuclear Collective Motion, Methuen, London, 1970.

[63] P. Ring and P. Schuck, *The Nuclear Many-Body Problem* (Springer, New York, 1980).

[64] J. Speth, E. Werner, and W. Wild, Phys. Rep. **33**, 127 (1977).

[65] D.J. Thouless, Nucl. Phys. **21**, 225 (1960); **22**, 78 (1961).

[66] G. Có and S. Krewald, Phys. Lett. **137B** (1984).

[67] L.D. Landau, Zh. Eksp. Teor. Fiz. **30**, 1058 (1956) [Sov. Phys. JETP **3**, 920 (1957)]; **32**, 59 (1957) [**5**, 101 (1957)]; **35**, 97 (1959) [**8**, 70 (1959)].

[68] A.B. Migdal, Nucl. Phys. **13**, 655 (1959).

[69] A.B. Migdal, *Theory of Finite Fermi Systems and Applications to Atomic Nuclei* (Wiley, New York, 1967).

[70] P.D. Kunz, The computer code DWUCK4 (unpublished).

[71] R.D. Smith and J. Wambach, Phys. Rev. C **38**, 100 (1988).

[72] F. Osterfeld, Rev. Mod. Phys. **64**, 491 (1992).

[73] H. Condé *et al.*, Nucl. Phys. **A545**, 785 (1992).

[74] W. Unkelbach, Ph.D. thesis, University of Bonn, Jül-2477, 1991.

(1985).